The “electric-dipole” effect of Pt–Ni for enhanced catalytic dehydrogenation of ammonia borane

Bin Wang, Laifei Xiong, Hanjing Hao, Hairui Cai, Pengfei Gao, Fuzhu Liu, Xiaojing Yu, Chao Wu, Shengchun Yang

PII: S0925-8388(20)32617-7

DOI: https://doi.org/10.1016/j.jallcom.2020.156253

Reference: JALCOM 156253

To appear in: *Journal of Alloys and Compounds*

Received Date: 2 April 2020

Revised Date: 24 June 2020

Accepted Date: 29 June 2020

Please cite this article as: B. Wang, L. Xiong, H. Hao, H. Cai, P. Gao, F. Liu, X. Yu, C. Wu, S. Yang, The “electric-dipole” effect of Pt–Ni for enhanced catalytic dehydrogenation of ammonia borane, *Journal of Alloys and Compounds* (2020), doi: https://doi.org/10.1016/j.jallcom.2020.156253.

CRediT authorship contribution statement:

Bin Wang: Conceptualization, Investigation, Writing - original draft, Funding acquisition. Laifei Xiong: Investigation. Hanjing Hao: Investigation. Hairui Cai: Formal analysis, Resources. Pengfei Gao: Formal analysis. Fuzhu Liu: Formal analysis. Xiaojing Yu: Validation, Resources. Chao Wu: Supervision, Writing - review & editing. Shengchun Yang: Supervision, Writing - review & editing.

Graphic Abstract

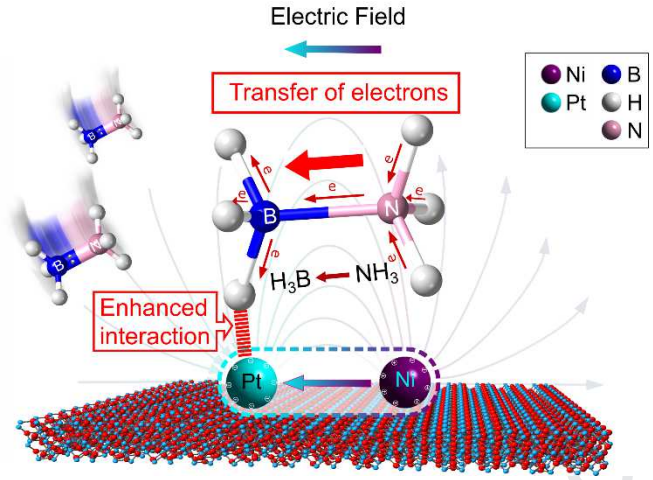

Title* The "electric-dipole" effect of Pt-Ni for enhanced catalytic dehydrogenation of ammonia borane

Bin Wang,[1,§,*] Laifei Xiong,[1,§] Hanjing Hao,[1,§]Hairui Cai,[1] Pengfei Gao,[2] Fuzhu Liu,[1] Xiaojing Yu,[3] Chao Wu[4,*], Shengchun Yang[1,*]

1. School of Science, MOE Key Laboratory for Non-equilibrium Synthesis and Modulation of Condensed Matter, State Key Laboratory for Mechanical Behavior of Materials, Xi'an Jiaotong University, Xi'an 710049, People's Republic of China
2. Northwest Institute of Nuclear Technology, Xi'an 710024, People's Republic of China
3. School of Materials Science and Engineering, Xi'an University of Technology, Xi'an 710048, People's Republic of China
4. Frontier Institute of Science and Technology, Xi'an Jiaotong University, Xi'an 710054, People's Republic of China

* Corresponding authors: bin_wang@xjtu.edu.cn; chaowu@mail.xjtu.edu.cn; ysch1209@mail.xjtu.edu.cn

§ These authors contributed equally.

Abstract

In this work, we prepared the PtNi alloy nanoparticles on Al_2O_3 (Al_2O_3-PtNi) *via* a simple wet-grinding method followed by a thermal reduction process. The as-prepared Al_2O_3-PtNi displayed a higher TOF of 426.84 mol_{H2} $(mol_{Pt}\cdot min)^{-1}$ toward the dehydrogenation of AB (ammonia borane) than Al_2O_3-Pt and Al_2O_3-Ni. Based on the theoretical calculations, an "electric-dipole" effect generated by the neighboring Pt-Ni atoms was found to facilitate the catalytic dehydrogenation process of ammonia borane (AB). The external electric field produced by the Pt-Ni dipole can elongate the B-H bond and increase the negative charges of H atoms on the BH_3 group, which helps to activate the B-H bond in the AB molecule, and thus enhances the kinetic

process of catalysis.

Keywords:

The “Electric-dipole” effect; Pt-Ni alloy nanoparticles; Electron transfer; Ammonia borane; Hydrogen evolution

1. Introduction

As a clean and source-independent energy carrier, hydrogen possesses a higher gravimetric energy density (120 MJ/kg) than gasoline (44 MJ/kg), and can be used to operate environment-friendly fuel cells with H_2O as the only byproduct[1]. However, it is still a challenge to controllably store and release 5-13 kg of H_2 to enable a 300-mile driving range with no excessive weight added to the fuel-cell-powered vehicle[2]. For this onboard H_2 storage in vehicular applications, the U.S. Department of Energy (DOE) set a gravimetric hydrogen capacity (GHC) of 5.5 wt% or volumetric hydrogen capacity (VHC) of 40 g/L as the target for the year 2025 and 6.5 wt% (50 g/L) as the ultimate target[3].

Among various approaches, such as compressed gas[4], liquid H_2[5], material absorption[6], *etc.*, chemical hydrogen storage in materials composed of light elements has drawn lots of attention. Ammonia borane (NH_3BH_3, AB), a stable, non-toxic, non-flammable B-N compound, is considered as one of the leading candidates for hydrogen storage due to its high GHC of 19.6 wt% and VHC of 140 g/L, which are greater than the U.S. DOE’s target. It has been reported that both hydrolysis[7] and thermolysis[8] can be performed to produce hydrogen from AB and the obtained final byproduct can also be utilized to regenerate AB[9]. Compared with thermolysis for 100% decomposition of AB at high temperature, the catalytic hydrolysis provides a convenient approach to release three equivalents of pure hydrogen from AB in the presence of an appropriate catalyst ($NH_3BH_3 + 2H_2O \rightarrow NH_4BO_2 + 3H_2$) at room temperature. Thus, it is highly desirable to develop excellent catalysts with high activity, reusability and large-scale facile preparation to meet the terminal practical requirements of this system in fuel cells.

Various noble metal catalysts like Rh, Pd, Ru nanoclusters, as well as the

supported noble metals (Ru, Rh, Pd, Pt, and Au) over Al_2O_3, C and SiO_2, have been widely studied to produce hydrogen by the hydrolysis of AB[10]. Among them, platinum-based catalysts have exhibited remarkable performance in this catalytic reaction. Chen et al. fabricated Pt-WO_3 with dual-active-sites to boost hydrogen evolution from ammonia borane for the first time[11]. In such unique catalyst, Pt and WO_3 acted as the active for ammonia borane and H_2O activation, respectively. However, the high cost and limited reserve of platinum greatly hindered their practical applications. Therefore, it is desirable to develop a low-cost catalyst with high hydrolysis activity. Recently, many non-noble metals, such as Ni, Co, Fe, etc., have been studied for the catalytic dehydrogenation of AB[5]. For example, Mahyari et al. prepared Ni nanoparticles immobilized on three-dimensional nitrogen-doped graphene-based frameworks with a TOF of 41.7 mol_{H2} mol_{Ni}^{-1} min^{-1} for the hydrolytic dehydrogenation of ammonia borane[9]. Hu et al. reported that Co nanoparticles supported by amine-rich polyethyleneimine and graphene oxide (PEI-GO/Co) showed an enhanced catalytic performance with a TOF of 39.9 mol_{H2} mol_{Co}^{-1} min^{-1} for hydrogen evolution from AB solution [12]. Although many attempts have been made to develop an efficient non-noble catalyst for catalytic hydrolysis AB, there still exists a catalytic activity gap between the noble metals and non-noble metals.

Another efficient strategy to develop low-cost catalysts is to minimize the usage of noble metal *via* introducing transition metals to form bimetallic nanoparticles (NPs) catalysts or core-shell structured catalyst[13-17]. Ge *et al.* developed a new strategy to synthesize PtNi/NiO clusters coated by small-sized hollow silica for highly efficient hydrogen evolution from the hydrolysis of NH_3BH_3[17]. Li *et al.* reported a galvanic replacement method to synthesize atomically dispersed Pt on the surface of Ni particles supported by CNT and found the dissociation of an O-H bond in H_2O is rate-determining step (RDS)[18]. Furthermore, based on the results of kinetic isotope effect (KIE) measurements, Li *et al.* confirmed that RDS for AB hydrolysis was the breaking of an O-H bond in H_2O[19]. Zhu et al. immobilized ultrafine AuNi alloy nanoparticles into MIL-101. The authors found that the AuNi/MIL-101 displayed a

high activity for hydrogen evolution from the catalytic hydrolysis of AB[20]. Core-shell structured Pt@Ni NPs were also synthesized by Qi et al. in hollow SiO_2 nanocapsules for the catalytic hydrolysis of AB[21]. It is well known that there is a strong electronic interaction between different metal atoms when introducing a second metal into the host metal due to the difference of their electronegativity[22, 23]. However, up to now, it is still unclear about the effect of electronic interaction between different metal atoms on the kinetics of AB hydrolysis.

In this work, by taking Al_2O_3 as catalyst support due to its low cost, high surface area, and high abundance[24], we synthesized Al_2O_3-PtNi with high catalytic activity and long-term durability for hydrogen generation from AB *via* a simple wet-grinding method followed by a thermal reduction process. Various characterizations, such as XRD, TEM, XPS, *etc*., were conducted to analyze the catalysts in-depth, and the kinetics of catalytic dehydrogenation of AB were studied systemically. An "electric-dipole" effect of neighboring Pt-Ni atoms was found to facilitate the catalytic dehydrogenation process of ammonia borane (AB). The as-prepared Al_2O_3-PtNi catalyst displayed a higher TOF of 426.84 mol_{H2} $(mol_{Pt}\cdot min)^{-1}$ toward the dehydrogenation of AB in contrast to Al_2O_3-Pt and Al_2O_3-Ni.

2. Experimental section

2.1 Materials:

Nickel chloride ($NiCl_2\cdot 6H_2O$) was purchased from Aladdin Ltd. (Shanghai, China). Ammonia borane (AB) and Aluminium oxide (Al_2O_3) were purchased from Tianjin Kemiou Chemical Reagent Co., Ltd. Nitric acid (HNO_3) was purchased from Tianjin Fuyu Fine Chemical Co., Ltd. Chloroplatinic acid was purchased from Kunming Institute of Precious Metals. The deionized water used in all of the experiments was 18.25 MΩ cm. All the chemical reagents used in the preparation were analytical grade and without any further purification.

2.2 Synthesis of Al_2O_3-PtNi, Al_2O_3-Pt and Al_2O_3-Ni

The Al_2O_3-PtNi were synthesized by a wet-gridding method followed by a thermal

reduction process. Typically, 500 mg of Al_2O_3 and 30.5 mg of $NiCl_2 \cdot 6H_2O$ were added into an agate mortar. Then, 0.658 mL 195 mM H_2PtCl_6 solution and 2 mL H_2O were added into the mixture. Subsequently, vigorous grind the mixture until the sample became a dry powder. The powder sample was placed in a tube furnace at 400°C under the H_2/Ar atmosphere for 2 h. After cooling, the sample was washed in deionized water several times and dried under 60°C in a vacuum oven for 5h. The final obtained powder was designated as Al_2O_3-PtNi. The Al_2O_3-Ni and Al_2O_3-Pt were prepared by the same process except for no addition of H_2PtCl_6 or $NiCl_2 \cdot 6H_2O$, respectively. The loadings of Pt and Ni in Al_2O_3-Pt and Al_2O_3-Ni were 5wt%. The Pt loading in Al_2O_3-PtNi was 5 wt%, consistent with that of Al_2O_3-Pt, and the molar ratio of Pt:Ni was 1:1.

2.3 Catalytic hydrolysis of AB

The procedure for catalytic hydrolysis of AB was conducted as previously reported[13, 25]. Typically, 50 mg catalyst was dispersed in 6 mL H_2O in a two-neck round-bottom flask, which was placed in a water bath at 25 ^oC, under continuous magnetic stir. The flash was purged with N_2 for 20 min and connected to an inverted measuring cylinder filled with water via a rubber tube. Then, 4 mL solution contained 2 mmol AB (corresponding to the generation of a maximum 6 mmol = 134 mL H_2 gas) was injected into the flask using a syringe. The volume of generated H_2 was measured by monitoring the displacement of water in the cylinder periodically. The reaction was stopped when no hydrogen generation was observed.

2.4 Calculation method

The turnover frequency (TOF) value was calculated by the following equation:

$$\mathrm{TOF} = \frac{n_{H2}}{n_{Pt} \times t} = \frac{V_{H2}}{22.4 \times n_{Pt} \times t} \qquad \text{Eq(1)}$$

where the n_{H2} is the mol of the generated hydrogen, n_{Pt} is the mol of Pt in the reaction system, V_{H2} is the volume of the generated hydrogen, and t is the reaction time. The unit of TOF in this work was $mol_{H2}\ mol_{Pt}^{-1}\ min^{-1}$.

The activation energy (E_a) for the catalytic hydrolysis of AB was evaluated based on the Arrhenius equation:

$$\ln K = \ln A - E_a/RT \quad \text{Eq(2)}$$

The rate constant K (mL/min) of H_2 evolution was determined by the volume of generated H_2 in the first 1 min for all catalysts, where the volume of evolved H_2 linearly increased with increasing reaction time. E_a is the activation energy. R is the gas constant. T is the reaction temperature.

2.5 Durability test of the catalyst

The process of durability test of the as-prepared catalyst was similar to the procedure of catalytic hydrolysis of AB. Typically, 50 mg catalyst was dispersed in 6 mL H_2O in a two-neck round-bottom flask under continuous magnetic stir. The first run was started when a 4 mL solution contained 2 mmol AB was injected into the flask using a syringe. The volume of generated H_2 was measured by monitoring the displacement of water in the cylinder periodically. After the completion of the 1st-run hydrolysis reaction, the catalyst was collected by centrifugation, washed with water. The obtained catalyst was reused for the next run of hydrolysis of AB. Such cycle tests were repeated 6 times.

2.6 Characterizations

The X-ray diffraction (XRD) patterns were obtained from a PANalytical X'pert MPD Pro diffractometer operated at 40 kV and 40 mA using Ni-filtered Cu Kα irradiation (Wavelength 1.5406 Å). The morphology was characterized by scanning electron microscope (SEM, JEOL JSM-7000F) at an acceleration voltage of 15 kV. The transmission electron microscopy (TEM) images, high-resolution TEM (HRTEM) images, and the high angle annular dark field-scanning transmission electron microscopy (HAADF-STEM) images were obtained from a JEOL JEM-F200 transmission electron microscope at an accelerating voltage of 200 kV. An OXFORDMAX-80 energy-dispersive X-ray detector (EDX) which was mounted in the above TEM was used to conduct elemental analysis. X-ray photoelectron spectroscopy (XPS) measurements were conducted on a Thermo Fisher ESCALAB Xi+ with monochromatic Al Kα radiation (hν = 1486.69 eV) and with the pressure of sample analysis chamber under high vacuum $<5\times10^{-10}$ mbar. All binding energies

were referenced to the C 1s peak at 284.8 eV. The total Pt and Ni contents in the as-prepared sample was measured by Inductively Coupled Plasma Mass Spectrometer (ICP-MS) (NexIONTM 350D, PerkinElmer, USA).

2.7 Theoretical methods

Spin-polarized DFT calculations were implemented by using the Vienna ab initial simulation package (VASP) with the projected augmented wave (PAW) potentials[26]. The Perfew-Burke_Ernzerhof (PBE) functional was used to describe the exchange-correlation potential[27]. The energy cutoff was set to 400 eV. A Monhorst-Pack k-point mesh of 3×3×1 was used for sampling the Brillouin zone for a (2×2) PtNi (1 1 1) supercell. Four atomic layers were included and the bottom two layers were fixed during the optimizations. A 15 Å vacuum layer was added to minimize the layer interactions. The converge criteria for energy and force are 10^{-4} eV and 0.05 eV/Å, respectively. The supercell models of PtNi and the AB molecule are shown in Figure S1-2, respectively.

The adsorption energy of molecule X (X = AB, H_2O) was calculated as:

$$E_{adsorption} = E_{(X+surf.)} - E_{surf.} - E_X \quad \text{Eq(3)}$$

where $E_{(X+surf.)}$, $E_{surf.}$ and E_X were the total energy of X adsorbed surface, clean surface and X molecule, respectively.

The MP2 method was applied by using Gaussian software package to explore the structure and properties of BH_3NH_3, the geometry of BH_3NH_3 were optimized in the external electric fields of 0 and 0.0320 a.u. (1 a.u. = 5.142×10^{11} V m^{-1}) at the MP2/6-311+G(2df,p) level[28]. The external electric field was applied along the direction from the N atom to the B atom. The natural bond orbital (NBO) analyses were conducted at the QCISD/aug-cc-pVTZ level.

3. Results and discussion

The Al_2O_3-PtNi catalysts were prepared *via* the wet-grinding method followed by a thermal reduction process. A simplified illustration of the synthesis process for Al_2O_3-PtNi is depicted in Figure 1a. Briefly, the precursor was obtained by grinding

the mixture of H_2PtCl_6, $NiCl_2$, Al_2O_3, and H_2O until the mixture became dry powder. Then, the as-prepared precursor was calcined under the H_2/Ar atmosphere at 400°C. The finally obtained powder was the Al_2O_3-PtNi catalyst. The morphology of the as-prepared Al_2O_3-PtNi was characterized by transmission electron microscopy (TEM). Figure 1a shows a representative TEM image of Al_2O_3-PtNi. It can be seen in Figure 1b that PtNi NPs with high contrast, which are indicated by white arrows, are well monodispersed on the surface of Al_2O_3. The TEM image of Al_2O_3-Pt in Figure S3a shows that the Pt nanoparticles were distributed on the surface of Al_2O_3, but some Pt nanoparticles were slightly aggregated on Al_2O_3 (Figure S3b). The average size of PtNi nanoparticles is measured to be *ca.* 2.4 ± 0.5 nm (Figure S4), which was smaller than that of Pt nanoparticle (2.8 ± 0.6 nm, Figure S3c). Compared with Pt nanoparticles in Al_2O_3-Pt, the smaller size and well-distribution of PtNi in Al_2O_3-PtNi should also be favorable to the hydrolysis of AB molecule. Figure 1c shows the enlarged TEM image of the dotted box in Figure 1b. The high-resolution TEM image (HRTEM) of PtNi (inset in Figure 1c), which is recorded from the rectangular area in Figure 1c, reveals a well-resolved lattice spacing of 0.21 nm, consistent with the (111) lattice spacing of the PtNi alloy.[29] The corresponding EDX spectrum (Figure S5) further confirmed the existence of Al, O, Pt and Ni elements in Al_2O_3-PtNi. Moreover, the HAADF-STEM image of Al_2O_3-PtNi and elemental mapping distribution were recorded in Figure 1d. It can be confirmed that the Al and O were uniformly distributed through the as-prepared Al_2O_3-PtNi. While Pt and Ni elements show the same distribution without the segregation of each other throughout the image area,

revealing the successful synthesis of homogeneous PtNi alloy nanoparticles that are deposited on the surface of Al_2O_3. Furthermore, inductively coupled plasma mass spectrometry (ICP-MS) characterization was conducted to analyze the Pt and Ni content in Al_2O_3-PtNi. The mass fractions of Pt and Ni elements were 5 % and 1.5%, respectively, suggesting that the atomic ratio of Pt/Ni was approximately 1:1.

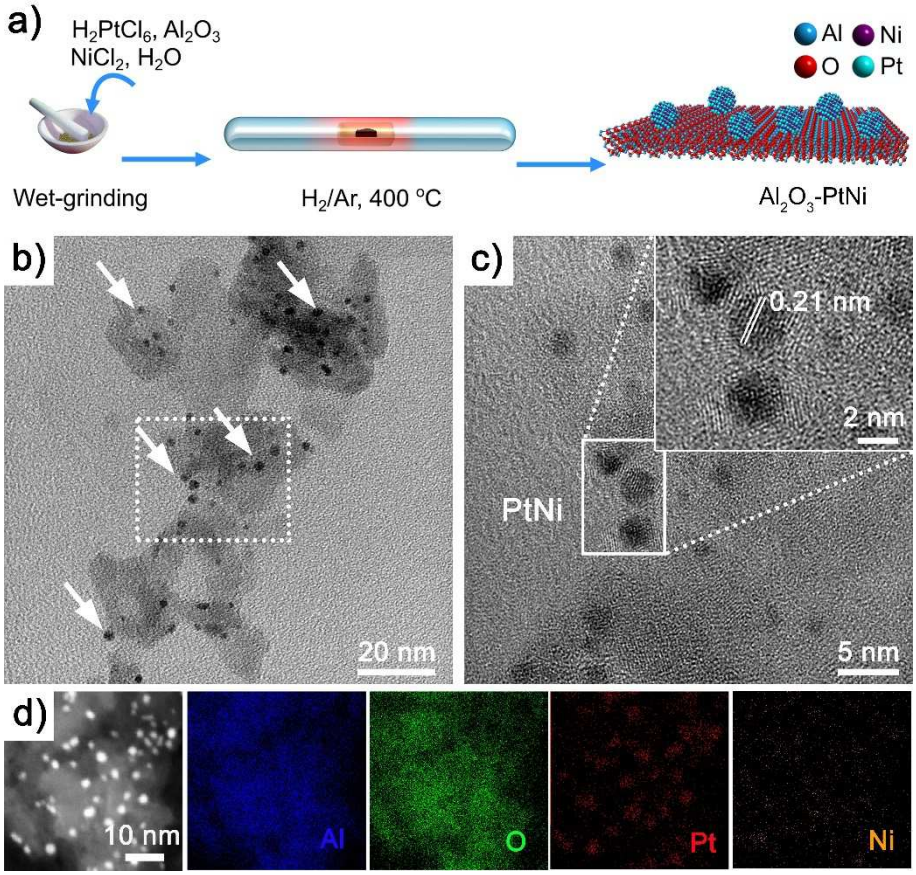

Figure 1. a) Schematic illustration of the synthesis process for Al_2O_3-PtNi. b) The TEM image of Al_2O_3-PtNi, the PtNi nanoparticles are indicated by white arrows; c) the enlarged TEM image of the dotted box area in a), the inset is the HRTEM image of the rectangular area in b); d) the HAADF-STEM image of Al_2O_3-PtNi and the corresponding EDX elemental mapping of Al, O, Pt and Ni, respectively.

The chemical state and surface characterization of Pt and Ni atoms in the as-prepared samples were investigated through X-ray photoelectron spectroscopy (XPS). All of the XPS signals of Pt, Ni, Al, and O were detected in the Al_2O_3-PtNi

sample (Figure S6). The high-resolution XPS spectra of Al 2p, Pt 4f regions for Al_2O_3-Pt and Al_2O_3-PtNi samples are shown in Figure 2a. The peaks located at 74.5 eV corresponds to the Al 2p of Al_2O_3[30-32], and no shift of the peak position for Al 2p is observed. The other peaks at around 71.3 eV can be assigned to Pt $4f_{7/2}$ of metallic Pt[33, 34], and the Pt $4f_{7/2}$ peak of Al_2O_3-PtNi shows a negative shift by 0.2 eV in contrast to that of Al_2O_3-Pt, suggesting a strong electron interaction between the Pt and Ni atoms in Al_2O_3-PtNi. However, the corresponding Pt $4f_{5/2}$ peaks of metallic Pt at around 74.6 eV were not observed due to the weak peaks of Pt $4f_{5/2}$ overlapped by the strong peaks of Al 2p at 74.5 eV. The high-resolution XPS spectra of Ni 2p for Al_2O_3-Ni and Al_2O_3-PtNi (Figure 2b) is well fitted with two spin-orbit doublets of Ni $2p_{3/2}$ and Ni $2p_{1/2}$ at around 855.8 and 874.8 eV, respectively. The peaks at *ca.* 880.1 and 862.5 eV with intense signals are the shake-up satellites arising from the multi-electron excitation[35]. Further deconvolution of Ni $2p_{3/2}$ and Ni $2p_{1/2}$ spectra for Al_2O_3-Ni reveal two different chemical environments for Ni. The peaks at 852.2 and 869.5 eV can be assigned to the metallic Ni(0), while the peaks located at 855.9 and 873.5 eV are ascribed to the Ni(II) oxidation state, which may be ascribed to the interaction between Ni and lattice O atom in Al_2O_3. Compared with Al_2O_3-Ni, the peak positions of Ni $2p_{3/2}$ and Ni $2p_{1/2}$ spectra for Al_2O_3-PtNi were positively shifted by 0.2 eV. When Pt was alloyed with Ni metal, an electron-withdrawing effect would be occurred from Ni atoms to Pt atoms due to the larger electronegativity of Pt (2.28) than that of Ni (1.91), thus resulting in the lower Pt binding energy and higher Ni binding energy of Al_2O_3-PtNi, respectively. Figure S7 shows the X-ray diffraction

patterns of the as-prepared samples. The XRD peak for PtNi(111) was detected, and the relatively low intensity of PtNi(111) than that of Pt(111) suggested the smaller size of PtNi in contrast to those of Pt, which was consistent with the result of TEM images for the two sample (Figure S3).

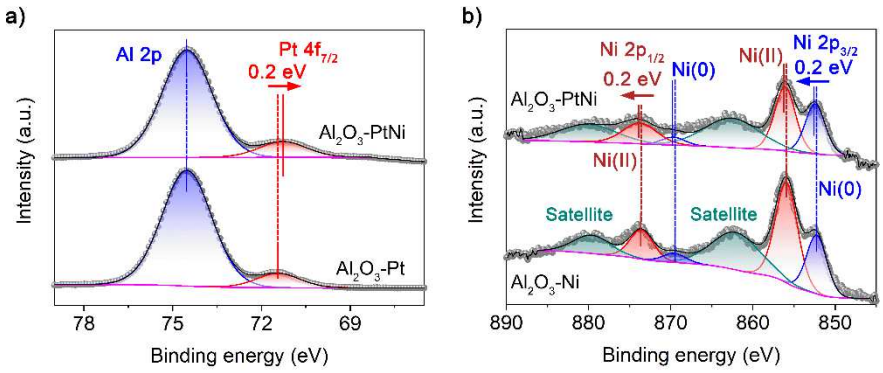

Figure 2. a) The high-resolution Al 2p & Pt 4f XPS profiles of Al_2O_3-PtNi and Al_2O_3-Pt, respectively; b) The high-resolution Ni 2p XPS profiles of Al_2O_3-PtNi and Al_2O_3-Ni, respectively.

It is well known that the dative bond of B-N in AB is formed by the donation of the N lone-pair electrons to the empty p-orbital of B[36]. The difference in electronegativity (χ) of the component hydrogen (χ_H=2.20), nitrogen (χ_N=3.04) and boron atoms (χ_B=2.04) result in the heterogeneous charge distribution in the NH_3BH_3 molecule[37, 38]. Thus, the H atoms attached to B are electronegative and those attached to N are electropositive[39-41]. As reported by Chandra *et al.*[42], during the catalytic dehydrogenation of AB in aqueous solution over metal catalyst, an activated complex species between AB and the metal surface was formed first and then it was immediately attacked by H_2O molecules, leading to the dissociation of the B-N bond. The resulted BH_3 intermediate was hydrolyzed quickly to release H_2 together with the formation of borate ion. It has been reported that the metal catalyst surface can react with the H atom within AB molecules to form the activated complex species, which is the prerequisite to generate hydrogen[13, 43, 44]. Based on the above dehydrogenation process of AB, a plausible mechanism of catalytic hydrogen evolution from AB over Al_2O_3-PtNi is proposed, as shown in Figure 3. As evidenced

by the XPS result in Figure 2, electron naturally transfers from a less electronegative Ni atom to a more electronegative Pt atom, forming an electric dipole between the neighboring Pt-Ni atom pair (Figure 3, left). The newly generated local electric field from the Pt-Ni dipole could affect the electron distribution in the AB molecule (Figure 3, middle), and the electron-redistributed AB molecule may be more easily interacted with the PtNi catalyst to form the activated complex(Figure 3, right). Consequently, under the effect of Pt-Ni electric dipole, Al_2O_3-PtNi is believed to display higher catalytic activity toward the dehydrogenation of AB in contrast to Al_2O_3-Pt and Al_2O_3-Ni.

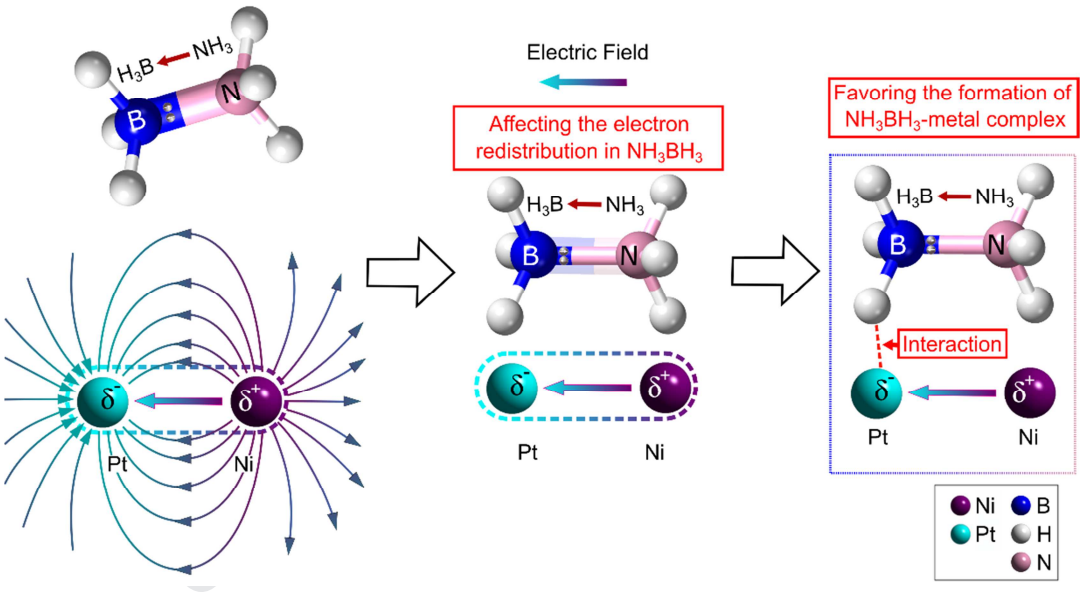

Figure 3. The plausible process of catalytic dehydrogenation of AB over Al_2O_3-PtNi with the help of the Pt-Ni dipole.

To verify the assumption mentioned above experimentally, the catalytic activity of the as-prepared Al_2O_3-Pt, Al_2O_3-Ni, and Al_2O_3-PtNi were evaluated by the catalytic dehydrogenation of AB tests. Briefly, 4 mL of AB solution (2 mmol, 500 mM) was added into a 6 mL dispersion of as-prepared catalyst. The H_2 gas generated from the catalytic hydrolysis of AB reaction was collected in a water-filled inverted measuring

cylinder and measured every ten seconds. Figure 4a shows the time course for hydrogen production from the hydrolysis of AB. No hydrogen was detected in the hydrolysis experiment over Al_2O_3-Ni even after 290 s, suggesting that Al_2O_3-Ni was inactive for the catalytic hydrolysis of AB in our case. For both Al_2O_3-Pt and Al_2O_3-PtNi, it was clear that no introduction periods were observed for the catalytic hydrolysis of AB over these two samples, and the molar ratio of generated H_2/AB was 3/1 during the catalytic course, revealing the complete dehydrogenation of AB. When Al_2O_3-Pt was used as catalyst, it took 270 s to 100% decompose AB with a TOF value of 95.07 $mol_{H2}\cdot(mol_{Pt}\cdot min)^{-1}$ (Table S1). Compared with Al_2O_3-Pt, Al_2O_3-PtNi provided a TOF of 315.17 $mol_{H2}\cdot(mol_{Pt}\cdot min)^{-1}$ (Table S1), which was *ca*. 3.32 times that of Al_2O_3-Pt, for the complete dehydrogenation of AB in only 90 s, providing solid evidence on the superior ability of Al_2O_3-PtNi toward catalytic hydrolysis of AB. This enhancement reasonably attributed to the effect of Pt-Ni electric dipole, which would be discussed later in this article in-depth. Since the durability of the catalyst is also a key parameter for its practical application, we also investigate the stability of Al_2O_3-PtNi by recycling the catalyst for six runs. As shown in Figure 4b, although the activity of Al_2O_3-PtNi showed a slight decrease, 100% AB was completely decomposed in 4 min even after 6 runs, demonstrating that Al_2O_3-PtNi possessed excellent durability during the recycling experiment. The slightly decreased activity of Al_2O_3-PtNi may be due to the loss of catalytic materials during the separation process of the catalyst after each run (the amount of catalyst was decreased from the initial 50 mg to final 43 mg after the sixth run).

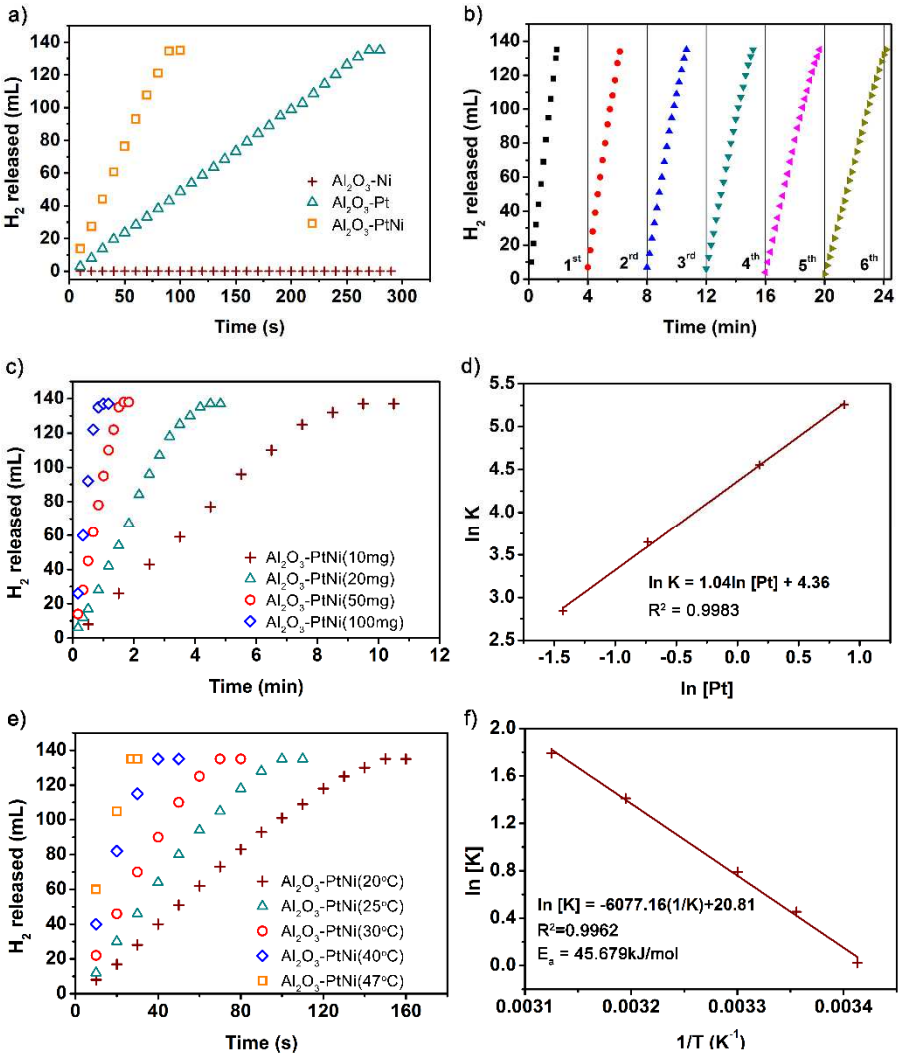

Figure 4. a) Time course for hydrogen production from AB over Al_2O_3-Pt, Al_2O_3-Ni, and Al_2O_3-PtNi, respectively; b) Durability test for the hydrogen generation from aqueous AB in the presence of Al_2O_3-PtNi catalyst; c) Plot of time *vs.* hydrogen evolution from AB hydrolysis over 10-100 mg Al_2O_3-PtNi at room temperature ([AB] = 200 mM); d) Plot of hydrogen generation rate *vs.* the concentration of Pt, both in logarithmic scale; e) Plot of time *vs.* the volume of hydrogen gas generated from AB hydrolysis by 50 mg Al_2O_3-PtNi at different temperatures; f) Arrhenius plot of ln[K] vs. the reciprocal reaction temperature 1/T in the temperature range of 20-47 ^{o}C.

To study the reaction kinetics of AB hydrolysis, the time courses of hydrogen evolution in the presence of Al_2O_3-PtNi with different mass were tested. When the mass usage of Al_2O_3-PtNi was 10 mg, 20 mg, 50 mg, and 100 mg, the concentration of Pt in the reaction solution was 0.24, 0.48, 1.20 and 2.40 mM, respectively. As

shown in Figure 4c, the time for completion of hydrolysis AB was decreased with the increase of catalyst mass from 10 to 100 mg, revealing that the increased concentration of Pt in the reaction solution can accelerate the hydrolysis rate of AB. Based on the results in Figure 4c, the reaction rates (K) can be determined from the linear portion of each plot. Figure 4d shows the relation between the reaction rates and the Pt concentration in logarithmic scale. It can be seen that the line slope is 1.04, clearly demonstrating that the hydrolysis of AB was first-order with respect to the Pt concentrations. Furthermore, we investigated the effect of temperature on the hydrogen evolution rate from the hydrolysis of AB. As shown in Figure 4e, the tests of catalytic hydrolysis of AB over Al_2O_3-PtNi were conducted at different temperatures in the range of 20 to 47 ^oC. It can be seen that the time for the completion of hydrolysis of AB was decreased from 160 to 30 s when the reaction temperature was increased from 20 to 47 ^oC, with the TOF increased from 199.19 to 1106.61 $mol_{H2} \cdot (mol_{Pt} \cdot min)^{-1}$ (Table S2), clearly confirming that temperature has a great influence on the hydrolysis kinetics of AB. Moreover, another parameter to assess the effectiveness of the catalyst is to evaluate its ability in reducing the activation barrier related to the hydrolysis of AB. Figure 4f shows the Arrhenius plots of ln[K] *vs.* the reciprocal reaction temperature 1/T in the temperature range of 20-47 ^oC. From the corresponding Arrhenius plots, the activation energy of Al_2O_3-PtNi was calculated to be 45.679 kJ/mol. When comparing with most reported Pt-based catalysts, our samples displayed a comparable catalytic performance in hydrolysis of AB, as shown in Table S3.

To further explore the role of the local electric field generated by the Pt-Ni dipole in the process of AB hydrolysis, a series of Density Functional Theory (DFT) calculations were conducted. Bader charge analysis revealed that *ca.* 0.3 e was transferred from Ni atoms to the neighboring Pt atoms in the (111) facet of PtNi, as shown in Figure S8, which led to the formation of Pt-Ni dipole, consistent with the XPS result (Figure 2). The absorption energy of AB and H_2O molecule on the (111) facet of PtNi was estimated to be ca. -0.919 eV and -0.195 eV, respectively (Table S4), revealing that AB molecule was preferentially absorbed on the PtNi (111) surface instead of H_2O molecule. It can be seen that one of the H atom on BH_3 group was bonded to a surface Pt atom (Figure 5a). In a free NH_3BH_3 molecule, the lengths of B-H bond and B-N bond are 1.209 Å and 1.649 Å, respectively (Table S7). Once the AB molecule absorbed on PtNi(111) surface, DFT calculations revealed that the B-H and B-N bond length are 1.361 Å and 1.602 Å, which are increased by 0.152 Å and decreased by 0.047 Å relative to the free molecule, respectively. This suggested that the B-H bond in the AB molecule was activated by priority. Further, the influence of the local electric field by the Pt-Ni dipole on the AB molecule was simulated by calculating the molecule in the external electric field of 0.032 a.u.. With the external electric field applied in the direction of the local field, more negative charges accumulated to the BH_3 group (-0.334 |e| to -0.422|e|, Table S5), which was transferred from NH_3 group *via* the "B-N bond" channel (Figure 5b). The increased negative charges in the H atom attached on B atom (-0.10690 |e| to -0.13776 |e|, Table S6) could enhance the interaction between AB molecules and the vacant 5d band of Pt in Pt-Ni dipole (Figure 5b), thus promoting the formation of the activated complex, which is the prerequisite to generate hydrogen[13, 43, 44]. The structure analysis indicated that the electric field (0.032 a.u.) from Ni atom to Pt atom made the B-N bond length shorter (1.649 Å to 1.613 Å, Table S7), but the B-H bond length became longer (1.209 Å to 1.224 Å, Table S7), suggesting that the local electric field can also activate the B-H bond in AB molecule. These analyses suggested that the activation of AB molecule on the PtNi catalyst can be attributed to the local electric field assisted

electronic structure of PtNi, thus enhancing the kinetic process of catalysis.

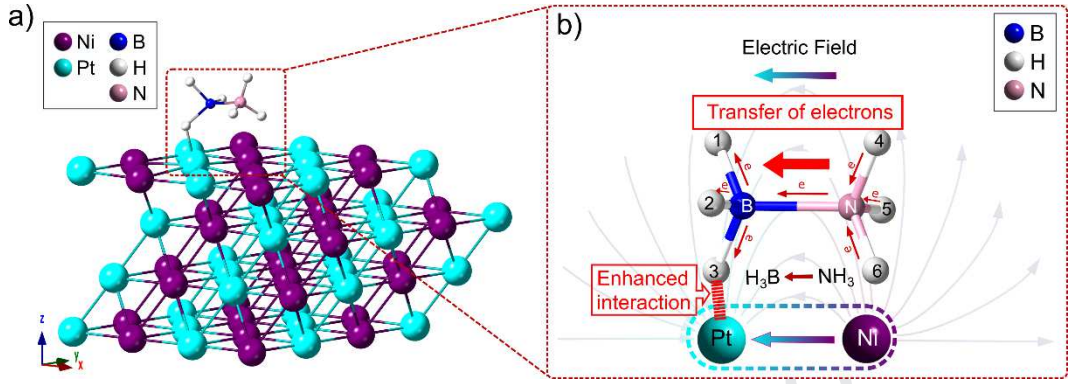

Figure 5. a) The adsorption configuration of AB molecule on PtNi (111) surface and b) the proposed mechanism for the effect of Pt-Ni dipole on the hydrolysis of AB.

4. Conclusion

In summary, compared with Al_2O_3-Pt, the TOF value toward the dehydrogenation of AB was greatly enhanced when introducing the Ni into Pt atoms to form PtNi alloy on Al_2O_3. Due to the larger electronegativity of Pt than that of Ni atoms, the electron donation from Ni atoms to Pt atoms led to the formation of electric dipole between a neighboring Pt-Ni atom pair. In the external local field generated by the Pt-Ni dipole, the redistribution of electrons in AB molecule resulted in the elongated B-H bond length and the increased negative charges in the H atom on BH_3 group, contributing to the activation of the B-H bond and the enhanced interaction between the AB molecule and the Pt atom in Pt-Ni dipole. Therefore, this unique “electric-dipole” effect was the reason for the higher catalytic activity of Al_2O_3-PtNi toward the dehydrogenation of AB in contrast to Al_2O_3-Pt and Al_2O_3-Ni. This work shed a light on the catalytic process of the molecule with a permanent dipole under the local field generated from the electric dipole on the surface of alloy catalyst.

Acknowledgments

This work is supported by National Natural Science Foundation of China (No. 51802255), the National Key Research and Development Program of China

(2017YFE0193900), Key Scientific and Technological Innovation Team of Shaanxi province(2020TD-001), China Postdoctoral Science Foundation (No. 2017M623161), the China Fundamental Research Funds for the Central Universities, and the Fundamental Research Funds and the World-Class Universities (Disciplines) and the Characteristic Development Guidance Funds for the Central Universities. The theoretical calculations were performed using the HPC Platform of Xi'an Jiaotong University. We thank Liqun Wang, Xiaojing Zhang and Chao Li for the help of data analyses, and we also thank the characterization support, such as TEM, XPS, ICP-MS, from the Instrument Analysis Center of Xi'an Jiaotong University.

References

[1] H. Zhang, J. Nai, L. Yu, X.W.D. Lou, Metal-organic-framework-based materials as platforms for renewable energy and environmental applications, Joule, 1 (2017) 77-107. https://doi.org/10.1016/j.joule.2017.08.008.

[2] B. Zohuri, Hydrogen Storage Processes and Technologies, Hydrogen Energy, Springer, Cham2019, pp. 257-279.

[3] M.D. Allendorf, Z. Hulvey, T. Gennett, A. Ahmed, T. Autrey, J. Camp, E. Seon Cho, H. Furukawa, M. Haranczyk, M. Head-Gordon, S. Jeong, A. Karkamkar, D.-J. Liu, J.R. Long, K.R. Meihaus, I.H. Nayyar, R. Nazarov, D.J. Siegel, V. Stavila, J.J. Urban, S.P. Veccham, B.C. Wood, An assessment of strategies for the development of solid-state adsorbents for vehicular hydrogen storage, Energy Environ. Sci., 11 (2018) 2784-2812. https://doi.org/10.1039/C8EE01085D.

[4] M. Jordá-Beneyto, F. Suárez-García, D. Lozano-Castelló, D. Cazorla-Amorós, A. Linares-Solano, Hydrogen storage on chemically activated carbons and carbon nanomaterials at high pressures, Carbon, 45 (2007) 293-303. https://doi.org/10.1016/j.carbon.2006.09.022.

[5] W.-W. Zhan, Q.-L. Zhu, Q. Xu, Dehydrogenation of Ammonia Borane by Metal Nanoparticle Catalysts, ACS Catal., 6 (2016) 6892-6905. https://doi.org/10.1021/acscatal.6b02209.

[6] L.J. Murray, M. Dincă, J.R. Long, Hydrogen storage in metal–organic frameworks, Chem. Soc. Rev., 38 (2009) 1294-1314. https://doi.org/10.1039/B802256A.

[7] M. Chandra, Q. Xu, A high-performance hydrogen generation system: Transition metal-catalyzed dissociation and hydrolysis of ammonia–borane, J. Power Sources, 156 (2006) 190-194. https://doi.org/10.1016/j.jpowsour.2005.05.043.

[8] Z. Li, G. Zhu, G. Lu, S. Qiu, X. Yao, Ammonia borane confined by a metal− organic framework for chemical hydrogen storage: enhancing kinetics and eliminating ammonia, J. Am. Chem. Soc., 132 (2010) 1490-1491. https://doi.org/10.1021/ja9103217.

[9] M. Mahyari, A. Shaabani, Nickel nanoparticles immobilized on three-dimensional nitrogen-doped graphene as a superb catalyst for the generation of hydrogen from the hydrolysis of ammonia borane, J. Mater. Chem. A, 2 (2014) 16652-16659. https://doi.org/10.1039/C4TA03940H.

[10] P.-Z. Li, Q. Xu, Metal-Nanoparticle Catalyzed Hydrogen Generation from Liquid-Phase Chemical Hydrogen Storage Materials, J. Chin. Chem. Soc., 59 (2012) 1181-1189. https://doi.org/10.1002/jccs.201200033.

[11] W. Chen, W. Fu, G. Qian, B. Zhang, D. Chen, X. Duan, X. Zhou, Synergistic Pt-WO_3 Dual Active Sites to Boost Hydrogen Production from Ammonia Borane, iScience, 23 (2020) 100922. https://doi.org/10.1016/j.isci.2020.100922.

[12] J. Hu, Z. Chen, M. Li, X. Zhou, H. Lu, Amine-Capped Co Nanoparticles for Highly Efficient Dehydrogenation of Ammonia Borane, ACS Appl. Mater. Interfaces, 6 (2014) 13191-13200. https://doi.org/10.1021/am503037k.

[13] K. Mori, K. Miyawaki, H. Yamashita, Ru and Ru-Ni nanoparticles on TiO_2 support as extremely active catalysts for hydrogen production from ammonia-borane, ACS Catal., 6 (2016) 3128-3135. https://doi.org/10.1021/acscatal.6b00715.

[14] X. Li, C. Zeng, G. Fan, Ultrafast hydrogen generation from the hydrolysis of ammonia borane catalyzed by highly efficient bimetallic RuNi nanoparticles stabilized on $Ti_3C_2X_2$ (X= OH and/or F), Int. J. Hydrog. Energy, 40 (2015) 3883-3891. https://doi.org/10.1016/j.ijhydene.2015.01.122.

[15] J. Shen, N. Cao, Y. Liu, M. He, K. Hu, W. Luo, G. Cheng, Hydrolytic dehydrogenation of amine-boranes catalyzed by graphene supported rhodium–nickel nanoparticles, Catal. Commun., 59 (2015) 14-20. https://doi.org/10.1016/j.catcom.2014.09.042.

[16] L. Guo, X. Gu, K. Kang, Y. Wu, J. Cheng, P. Liu, T. Wang, H. Su, Porous nitrogen-doped carbon-immobilized bimetallic nanoparticles as highly efficient catalysts for hydrogen generation from hydrolysis of ammonia borane, J. Mater. Chem. A, 3 (2015) 22807-22815. https://doi.org/10.1039/C5TA05487G.

[17] Y. Ge, W. Ye, Z.H. Shah, X. Lin, R. Lu, S. Zhang, PtNi/NiO Clusters Coated by Hollow Sillica: Novel Design for Highly Efficient Hydrogen Production from Ammonia–Borane, ACS Appl. Mater. Interfaces, 9 (2017) 3749-3756. https://doi.org/10.1021/acsami.6b15020.

[18] Z. Li, T. He, D. Matsumura, S. Miao, A. Wu, L. Liu, G. Wu, P. Chen, Atomically Dispersed Pt on the Surface of Ni Particles: Synthesis and Catalytic Function in Hydrogen Generation from Aqueous Ammonia-Borane, ACS Catal., 7 (2017) 6762-6769. https://doi.org/10.1021/acscatal.7b01790.

[19] Z. Li, T. He, L. Liu, W. Chen, M. Zhang, G. Wu, P. Chen, Covalent triazine framework supported non-noble metal nanoparticles with superior activity for catalytic hydrolysis of ammonia borane: from mechanistic study to catalyst design, Chem. Sci., 8 (2017) 781-788. https://doi.org/10.1039/C6SC02456D.

[20] Q.-L. Zhu, J. Li, Q. Xu, Immobilizing Metal Nanoparticles to Metal–Organic Frameworks with Size and Location Control for Optimizing Catalytic Performance, J. Am. Chem. Soc., 135 (2013) 10210-10213. https://doi.org/10.1021/ja403330m.

[21] X. Qi, X. Li, B. Chen, H. Lu, L. Wang, G. He, Highly Active Nanoreactors: Patchlike or Thick Ni Coating on Pt Nanoparticles Based on Confined Catalysis, ACS Appl. Mater. Interfaces, 8 (2016) 1922-1928. https://doi.org/10.1021/acsami.5b10083.

[22] L. Xiong, B. Wang, H. Cai, T. Yang, L. Wang, S. Yang, Neighboring effect induced by V and Cr doping in FeCoP nanoarrays for the hydrogen evolution reaction with Pt-like performance, J. Mater. Chem. A, 8 (2020) 1184-1192. https://doi.org/10.1039/C9TA12562K.

[23] S.T. Hunt, M. Milina, A.C. Alba-Rubio, C.H. Hendon, J.A. Dumesic, Y. Román-Leshkov,

Self-assembly of noble metal monolayers on transition metal carbide nanoparticle catalysts, Science, 352 (2016) 974-978. https://doi.org/10.1126/science.aad8471.

[24] T. Van Cleve, D. Underhill, M. Veiga Rodrigues, C. Sievers, J.W. Medlin, Enhanced Hydrothermal Stability of γ-Al_2O_3 Catalyst Supports with Alkyl Phosphonate Coatings, Langmuir, 34 (2018) 3619-3625. https://doi.org/10.1021/acs.langmuir.8b00465.

[25] Y. Ge, Z.H. Shah, X.-J. Lin, R. Lu, Z. Liao, S. Zhang, Highly Efficient Pt Decorated CoCu Bimetallic Nanoparticles Protected in Silica for Hydrogen Production from Ammonia-Borane, ACS Sustain. Chem. Eng., 5 (2017) 1675-1684. https://doi.org/10.1021/acssuschemeng.6b02430.

[26] J.P. Perdew, K. Burke, M. Ernzerhof, Generalized Gradient Approximation Made Simple, Phys. Rev. Lett., 77 (1996) 3865-3868. https://doi.org/10.1103/PhysRevLett.77.3865.

[27] G. Kresse, J. Furthmüller, Efficient iterative schemes for ab initio total-energy calculations using a plane-wave basis set, Phys. Rev. B, 54 (1996) 11169-11186. https://doi.org/10.1103/PhysRevB.54.11169.

[28] X. Zhang, S.-L. Sun, H.-L. Xu, Z.-M. Su, Ammonia borane in an external electric field: structure, charge transfer, and chemical bonding, RSC Adv., 5 (2015) 65991-65997. https://doi.org/10.1039/C5RA10156E.

[29] M. Li, Z. Zhao, T. Cheng, A. Fortunelli, C.-Y. Chen, R. Yu, Q. Zhang, L. Gu, B. Merinov, Z. Lin, E. Zhu, T. Yu, Q. Jia, J. Guo, L. Zhang, W.A. Goddard, Y. Huang, X. Duan, Ultrafine jagged platinum nanowires enable ultrahigh mass activity for the oxygen reduction reaction, Science, 354 (2016) 1414-1419. https://doi.org/10.1126/science.aaf9050.

[30] G. Shao, Y. Lu, X. Wu, J. Wu, S. Cui, J. Jiao, X. Shen, Preparation and thermal shock resistance of high emissivity molybdenum disilicide-aluminoborosilicate glass hybrid coating on fiber reinforced aerogel composite, Appl. Surf. Sci., 416 (2017) https://doi.org/10.1016/j.apsusc.2017.04.184.

[31] N. Batra, J. Gope, Vandana, J. Panigrahi, R. Singh, P.K. Singh, Influence of deposition temperature of thermal ALD deposited Al_2O_3 films on silicon surface passivation, AIP Adv., 5 (2015) 067113. https://doi.org/10.1063/1.4922267.

[32] M.Y. Smirnov, A.V. Kalinkin, V.I. Bukhtiyarov, X-ray photoelectron spectroscopic study of the interaction of supported metal catalysts with NO_x, J. Struct. Chem., 48 (2007) 1053-1060. https://doi.org/10.1007/s10947-007-0170-1.

[33] G. Bilger, M. Specht, C.U. Maier, A. Eicke, M. Gillmann, XPS-characterization of hydrogen-evolving platinum-coated p-silicon photoelectrodes, Appl. Surf. Sci., 75 (1994) 157-163. https://doi.org/10.1016/0169-4332(94)90153-8.

[34] L. Zhang, C. Jia, S. He, Y. Zhu, Y. Wang, Z. Zhao, X. Gao, X. Zhang, Y. Sang, D. Zhang, Hot Hole Enhanced Synergistic Catalytic Oxidation on Pt-Cu Alloy Clusters, Adv. Sci., 4 (2017) 1600448. https://doi.org/10.1002/advs.201600448.

[35] J. Wang, Q. Zhao, H. Hou, Y. Wu, W. Yu, X. Ji, L. Shao, Nickel nanoparticles supported on nitrogen-doped honeycomb-like carbon frameworks for effective methanol oxidation, RSC Adv., 7 (2017) 14152-14158. https://doi.org/10.1039/C7RA00590C.

[36] B. Yuan, J.-W. Shin, E.R. Bernstein, Dynamics and fragmentation of van der Waals and hydrogen bonded cluster cations:$(NH_3)_n$ and $(NH_3BH_3)_n$ ionized at 10.51 eV, J. Chem. Phys., 144 (2016) 144315. https://doi.org/10.1063/1.4945624.

[37] U.B. Demirci, Ammonia borane, a material with exceptional properties for chemical hydrogen storage, Int. J. Hydrog. Energy, 42 (2017) 9978-10013.

https://doi.org/10.1016/j.ijhydene.2017.01.154.
[38] J.-F. Petit, U.B. Demirci, Mechanistic Insights into Dehydrogenation of Partially Deuterated Ammonia Borane NH_3BD_3 Being Heating to 200 °C, Inorg. Chem., 58 (2019) 489-494. https://doi.org/10.1021/acs.inorgchem.8b02721.
[39] X.-M. Chen, S.-C. Liu, C.-Q. Xu, Y. Jing, D. Wei, J. Li, X. Chen, Unravelling a general mechanism of converting ionic B/N complexes into neutral B/N analogues of alkanes: $H^{\delta+}\cdots H^{\delta-}$ dihydrogen bonding assisted dehydrogenation, Chem. Commun., 55 (2019) 12239-12242. https://doi.org/10.1039/C9CC07133D.
[40] L. Gao, H. Fang, Z. Li, X. Yu, K. Fan, Liquefaction of Solid-State BH_3NH_3 by Gaseous NH_3, Inorg. Chem., 50 (2011) 4301-4306. https://doi.org/10.1021/ic200373g.
[41] X. Chen, J.-C. Zhao, S.G. Shore, The Roles of Dihydrogen Bonds in Amine Borane Chemistry, Acc. Chem. Res., 46 (2013) 2666-2675. https://doi.org/10.1021/ar400099g.
[42] Q. Xu, M. Chandra, Catalytic activities of non-noble metals for hydrogen generation from aqueous ammonia–borane at room temperature, J. Power Sources, 163 (2006) 364-370. https://doi.org/10.1016/j.jpowsour.2006.09.043.
[43] W. Chen, D. Li, Z. Wang, G. Qian, Z. Sui, X. Duan, X. Zhou, I. Yeboah, D. Chen, Reaction mechanism and kinetics for hydrolytic dehydrogenation of ammonia borane on a Pt/CNT catalyst, AIChE J., 63 (2017) 60-65. https://doi.org/10.1002/aic.15389.
[44] X. Yang, F. Cheng, Z. Tao, J. Chen, Hydrolytic dehydrogenation of ammonia borane catalyzed by carbon supported Co core–Pt shell nanoparticles, J. Power Sources, 196 (2011) 2785-2789. https://doi.org/10.1016/j.jpowsour.2010.09.079.

Highlights

- An electric dipole is formed between the neighboring Pt and Ni atom.
- The Pt-Ni dipole generates a local external electric field.
- The electric field increases negative charges in H atoms on BH_3 group and B-H length.
- The electric field helps to improve the interaction between AB molecule and Pt atom.
- The electric dipole effect leads to the higher catalytic activity of Al_2O_3@PtNi.

Declaration of interests

☒ The authors declare that they have no known competing financial interests or personal relationships that could have appeared to influence the work reported in this paper.

☐The authors declare the following financial interests/personal relationships which may be considered as potential competing interests: